We are IntechOpen, the world's leading publisher of Open Access books Built by scientists, for scientists

4,800
Open access books available

122,000
International authors and editors

135M
Downloads

Our authors are among the

154
Countries delivered to

TOP 1%
most cited scientists

12.2%
Contributors from top 500 universities

WEB OF SCIENCE™

Selection of our books indexed in the Book Citation Index in Web of Science™ Core Collection (BKCI)

Interested in publishing with us?
Contact book.department@intechopen.com

Numbers displayed above are based on latest data collected.
For more information visit www.intechopen.com

Chapter 8

Nano-Plasmonic Filters Based on Tooth-Shaped Waveguide Structures

Xu Guang Huang and Jin Tao

Additional information is available at the end of the chapter

http://dx.doi.org/10.5772/75765

1. Introduction

Along with development of human society and technology, it becomes more dependable on the miniaturization and integration of semiconductor components, circuits and devices. The performance of integrated circuits, such as micro-processor, is in accordance with the famous Moore's law that the number of transistors placed inexpensively on an integrated circuit doubles approximately every two years. However, the integration of modern electronic components and devices for information communication and processing have been approaching its fundamental speed and bandwidth limitation, because the ultra-intensive electrical interconnects have an increased effective resistor-capacitor (RC) time constant that increases the time of charging and discharging [1, 2]. This has caused an increasing serious problem that hinders further development in many fields of modern science and technology. Using light signals instead of electronic is one of the most promising solutions. The speed of optical signal is on the order of 10^8 m/s, which is about 3 orders of the saturation velocity of electrons in a semiconductor such as silicon [3]. However, a major problem with using light as information carrier in conventional optical devices is the poor performance of integration and miniaturization. Dielectric waveguides are basic components and cannot allow the localization of electromagnetic waves into subwavelength-scale regions because of diffraction limit $\lambda_0/2n$, here λ_0 is the wavelength of the light in the free space and n is the refractive index of the dielectric. Photonic crystal (PC) structures and devices have been studied by many researchers since E. Yablonovitch and S. John ' s two milestone published papers in 1987 [4, 5], which confirmed that the light can be confined in the nanoscale. However, the dimensions of the PC system are on the order of the wavelength or even larger, making them less appropriate for nano-scale optical elements integration.

Surface Plasmon polaritons (SPPs) are electromagnetic waves that propagate along the interface of metal and dielectric. In recent years, plasmonics is called the area of

nanophotonics under the light diffraction limit that studies the transmission characteristics, localization, guiding of the SPP mode using metallic nanosturctures. The plasmonic waveguides are the most basic components and have been given much attention. Various kinds of metallic nanostructures have been proposed for SPP guiding. Generally these structures could be classified into three big categories: 1) chains of metal nanoparticles [6] and cylindrical metallic nanorods with various geometries [7]. 2) Metal-dielectirc-metal (MDM) or Metal-insulator-metal (MIM) plasmonic waveguides, including groove channel structures in metallic substrates [8], slot waveguide [9]. 3) Dielectric-metal-dielectric (DMD)/ Insulator-metal-Insulator (IMI) waveguide [10]. It should be noted that not all these plasmonic structures can be used for guiding SPP mode to achieve subwavelength localization. Among them, MDM/MIM plasmonic waveguide can propagate SPP mode in the subwavelength scale with relatively low dissipation and large propagation distance. Our following proposed structures are mainly based on the MDM/MIM structures.

Wavelength selection is one of key technologies in fields of optical communication and computing. To achieve wavelength filtering characteristics, plasmonic Bragg reflectors and nanocavities have been proposed. They include the metal hetero-structures constructed with several periodic slots vertically along a metal-dielectric-metal (MDM) waveguide [11], the Bragg grating fabricated by periodic modulating the thickness of thin metal stripes embedded in an insulator [12] and the periodic structure formed by changing alternately two kinds of the insulators [13,14]. Lately, a high-order plasmonic Bragg reflector with a periodic modulation of the core index of the insulators [15], and a structure with periodic variation of the width of the dielectric in MDM waveguide [16] have been proposed. Most of the periodic structures mentioned above, however, have total length of micrometers and relatively high propagation loss of several decibels.

In this chapter, we present our recent work on compact nano-plasmonic waveguide filters based on T-series and nano-capillary structures. In section 2, we introduce the novel nanometeric plasmonic filter in a tooth-shaped MIM waveguide and give an analytic model based on the scattering matrix method. In section 3, we investigate the characteristics of double-side teeth-shaped nano-plasmonic waveguide. In section 4 and section 5, we introduce the multiple multiple-teeth-shaped plasmonic filters and asymmetrical multiple teeth-shaped narrow pass band subwavelength filter. In section 6, we introduce a wavelength demultiplexing structure based on metal-dielectric-metal plasmonic nano-capillary resonators. Finally, we make a conclusion.

2. Single-tooth shaped plasmonic waveguide filter [17]

To begin with the dispersion relation of the fundamental TM mode in a MIM waveguide (shown in the inset of Fig. 1) is given by [18]:

$$\varepsilon_{in} k_{z2} + \varepsilon_m k_{z1} \coth(-\frac{ik_{z1}}{2} w) = 0, \tag{1}$$

with k_{z1} and k_{z2} defined by momentum conservations:

$$k_{z1}^2 = \varepsilon_{in} k_0^2 - \beta^2, \quad k_{z2}^2 = \varepsilon_m k_0^2 - \beta^2 . \tag{2}$$

Where ε_{in} and ε_m are respectively dielectric constants of the insulator and the metal, $k_0=2\pi/\lambda_0$ is the free-space wave vector. The propagation constant β is represented as the effective index $n_{eff}=\beta/k_0$ of the waveguide for SPPs. The real part of n_{eff} of the slit waveguide as a function of the slit width at different wavelengths is shown in Fig. 1. It should be noted that the dependence of n_{eff} on waveguide width is also suitable to the region of the tooth waveguide with the tooth width of w_t shown in Fig. 2. The imaginary part of n_{eff} is referred to the propagation length which is defined as the length over which the power carried by the wave decays to 1/e of its initial value: $L_{spps}=\lambda_0/[4\pi\cdot\mathrm{Im}(n_{eff})]$. In the calculation above and the following simulations, the insulator in all of the structures is assumed to be air ($\varepsilon_{in}=1$), and the frequency-dependent complex relative permittivity of silver is characterized by Drude model: $\varepsilon_m(\omega)=\varepsilon_\infty-\omega_p^2/\omega(\omega+i\gamma)$. Here $\omega_p=1.38\times10^{16}\,Hz$ is the bulk plasma frequency, which represents the natural frequency of the oscillations of free conduction electrons. $\gamma=2.73\times10^{13}\,Hz$ is the damping frequency of the oscillations, ω is the angular frequency of the incident electromagnetic radiation, ε_∞ stands for the dielectric constant at infinite angular frequency with the value of 3.7 [16]

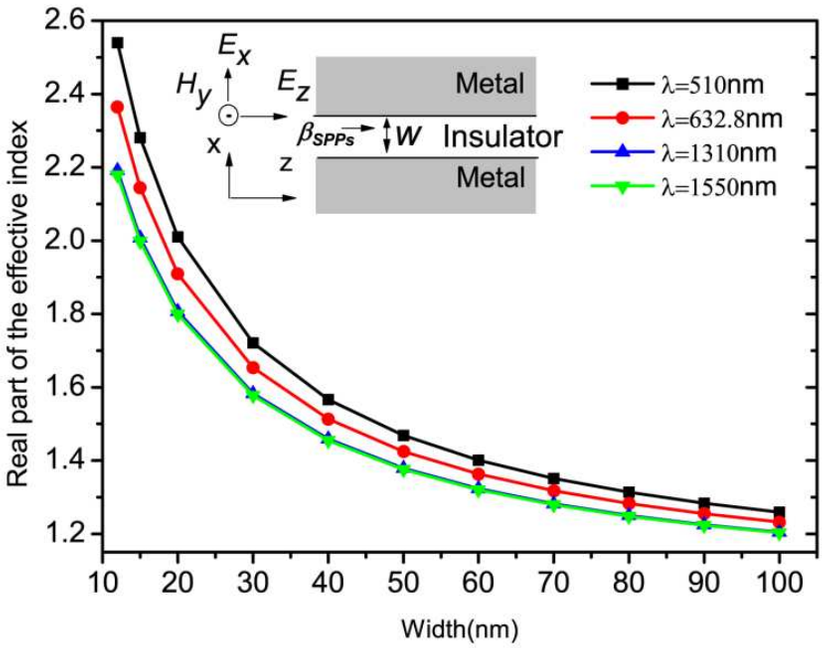

Figure 1. Real part of the effective of refraction index versus the width of a MIM slit waveguide structure.

The tooth-shaped waveguide filter is shown in Fig. 2. In the following FDTD simulations, the grid sizes in the x and z directions are chosen to be 5nm×5nm. Since the width of the waveguide is much smaller than the operating wavelength in the structure, only fundamental waveguide mode is supported. Two power monitors are respectively set at the

positions of P and Q to detect the incident and transmission fields for calculating the incident power of P_{in} and the transmitted power of P_{out}. The transmittance is defined to be $T=P_{out}/P_{in}$. The length of L is fixed to be 300nm, while the tooth width and depth are respectively w_t=50nm and d=100nm. The tabulation of the optical constants of silver [19] is used in the simulation. As shown in Fig. 3(a), the tooth-shaped waveguide is of a filtering function: A transmission dip occurs at the free space wavelength nearly 784nm with the transmittance of ~0%. The maximum transmittance at the wavelengths longer than 1700nm is over 90%. The contour profiles of the field distributions around the tooth-shaped area at different wavelengths are shown in Figs. 3(b)-3(d). The filtering structure is distinguished from the Bragg reflectors based on periodical heterostructure.

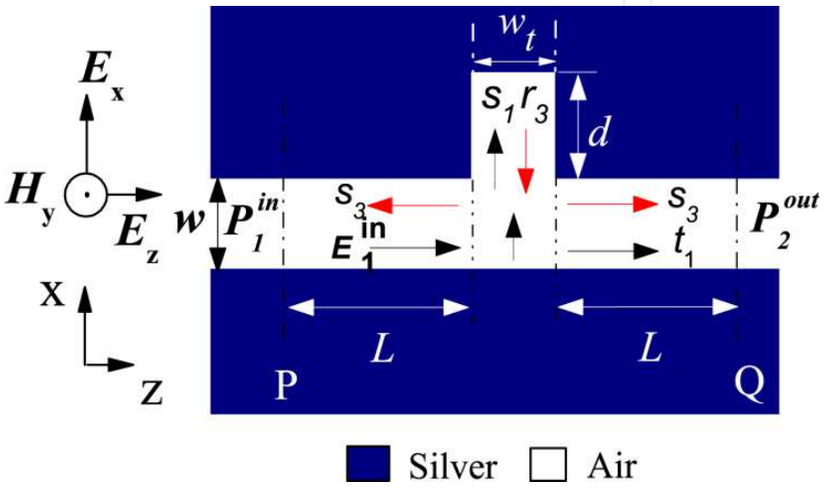

Figure 2. The structure schematic of a single tooth-shaped waveguide filter, with the slit width of w, the tooth width of w_t, and the tooth depth of d.

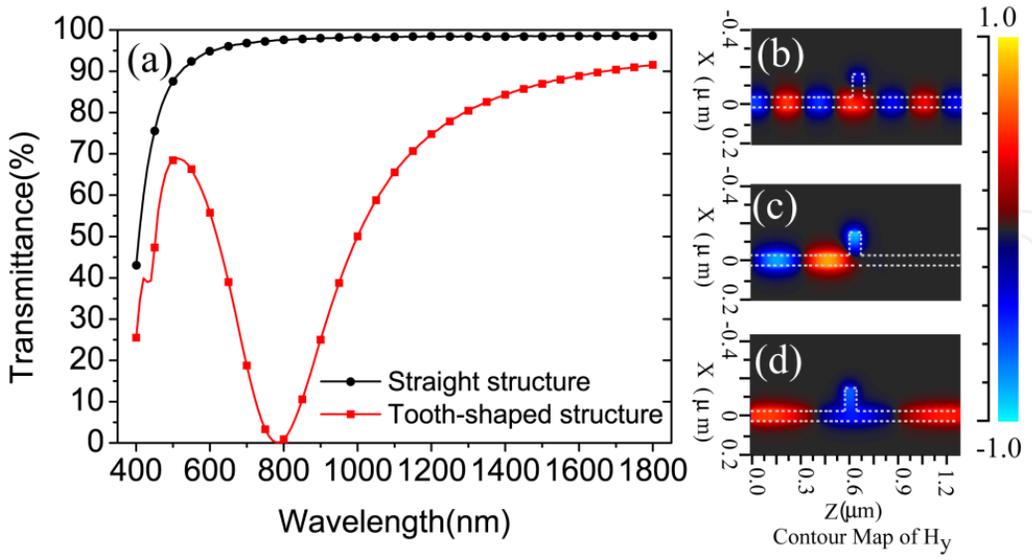

Figure 3. (a) Transmission of the single tooth-shaped MIM waveguide compared with a straight MIM slit waveguide. The width of the waveguide is w=50nm, and the tooth width and depth are respectively w_t=50nm and d=100nm. The contour profiles of field H_y of the tooth-shaped waveguide at different wavelengths of (b) λ=510nm, (c) λ=783nm, and (d) λ=1550nm.

The phenomenon above can be physically explained in the scattering matrix theory [20] as follows:

$$\begin{pmatrix} E_1^{\text{out}} \\ E_2^{\text{out}} \\ E_3^{\text{out}} \end{pmatrix} = S \cdot \begin{pmatrix} E_1^{\text{in}} \\ E_2^{\text{in}} \\ E_3^{\text{in}} \end{pmatrix}, \tag{3}$$

where $S = \begin{bmatrix} r_1 & t_1 & s_3 \\ t_1 & r_1 & s_3 \\ s_1 & s_1 & r_3 \end{bmatrix}$, r_i, t_i and s_i (i=1,2,3) are respectively the reflection, transmission and splitting coefficients of a incident beam from Port i (i=1,2,3), caused by the structure. E_{i}^{in} and $E_{\text{i}}^{\text{out}}$ stand for the fields of incident and output beams at Port i, respectively. Using the fact that $|S| = 1$, one can obtain:

$$r_1^2 r_3 + 2t_1 s_1 s_3 - 2r_1 s_1 s_3 - t_1^2 r_3 = 1. \tag{4}$$

For the case of $E_2^{\text{in}} = 0$, one has

$$E_2^{\text{out}} = t_1 E_1^{\text{in}} + s_3 E_3^{\text{in}}, \tag{5}$$

in which E_3^{in} is given as follows:

$$E_3^{\text{in}} = s_1 E_1^{\text{in}} \exp(i\phi(\lambda))(1 + r_3 \exp(i\phi(\lambda)) + r_3^2 \exp(2i\phi(\lambda)) + ...) = \frac{s_1 E_1^{\text{in}}}{1 - r_3 \exp(i\phi(\lambda))} \exp(i\phi(\lambda)), \tag{6}$$

where the phase delay $\phi(\lambda) = \frac{4\pi}{\lambda} n_{eff} \cdot d + \Delta\varphi(\lambda)$, and $\Delta\varphi(\lambda)$ is the phase-shift caused by the reflection on the air-silver surface. Combined Eq. (5) and Eq. (6), the output field at Port 2 is derived as:

$$E_2^{\text{out}} = t_1 E_1^{\text{in}} + \frac{s_1 s_3 E_1^{\text{in}}}{1 - r_3 \exp(i\phi(\lambda))} \exp(i\phi(\lambda)), \tag{7}$$

Therefore, the transmittance T from Port 1 to Port 2 is given by:

$$T = \left| \frac{E_2^{\text{out}}}{E_1^{\text{in}}} \right|^2 = \left| t_1 + \frac{s_1 s_3}{1 - r_3 \exp(i\phi(\lambda))} \exp(i\phi(\lambda)) \right|^2. \tag{8}$$

It can be seen from Eq. (8) that, if the phase satisfies $\phi(\lambda) = (2m+1)\pi$ (m=0,1,2…), the two terms inside the absolute value sign on the right of the equation will cancel each other (as it

can be seen in Fig. 3(c)), so that the transmittance T will become minimum. Therefore, the wavelength λ_m of the transmission dip is determined as follows:

$$\lambda_m = \frac{4 \cdot n_{eff} \cdot d}{(2m+1) - \frac{\Delta\varphi(\lambda)}{\pi}}. \tag{9}$$

It can be seen that the wavelength λ_m is linear to the tooth depth d, and depends on tooth width w_t, through the somewhat inverse-proportion-like relationship between n_{eff} and w_t shown in Fig. 1.

Figure 4(a) shows the transmission spectra of the waveguide filters with various tooth widths of w_t. The maximum transmittance can reach 97%. Figure 4(b) shows the wavelength of the trough vs. the tooth width of w_t. The primary dip of the transmission moves very significantly to short wavelength (blue-shift) with the increase of w_t for w_t<20nm. The shift rate rapidly becomes small after w_t>20nm, and tends to be saturated when w_t>200nm. As revealed in the Eq. (9), the above relationship between the dip position and w_t mainly results from the contribution of the inverse-proportion-like dependence of n_{eff} on w_t. The change rate of $\Delta n_{eff}/\Delta w_t$ within the tooth width of 20nm is much higher than that of $\Delta n_{eff}/\Delta w_t$ after w_t>20nm, as shown in Fig. 1, and becomes finally saturated after w_t>200nm. Obviously, tooth width w_t should be chosen within the range of 20-200nm to avoid the critical behavior and the difficulty in fabrication process.

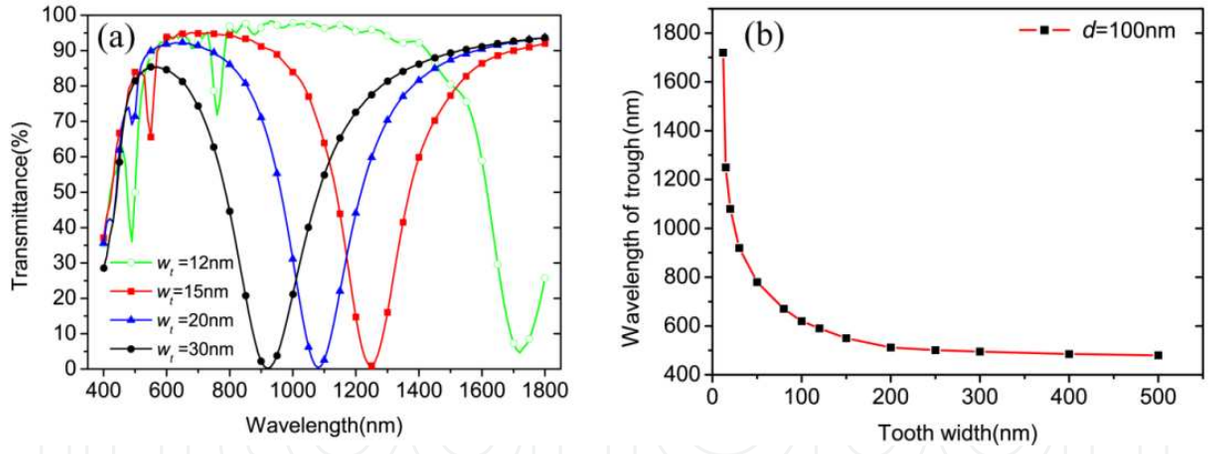

Figure 4. (a) Transmission spectra of the waveguide filters with various tooth widths of w_t, at a fixed tooth depth of d=100nm and the slit width of w=50nm. (b) The wavelength of the trough versus the tooth width of w_t.

Figure 5(a) shows the transmission spectra of the filters with different tooth depths of d. It is found that the wavelength of the transmission dip shifts to long wavelength with the increasing of d. Figure 5(b) reveals that the wavelength of the transmission dip has a linear relationship with the tooth depth, as our expectation in Eq. (9). Therefore, one can realize the filter function in various required wavelength with high performance by changing the width or/and the depth of the tooth. For example, to obtain a filter with a transmission dip at the wavelength of 1550nm, the structural parameters of w_t=w=50nm and d=237.5nm can be chosen.

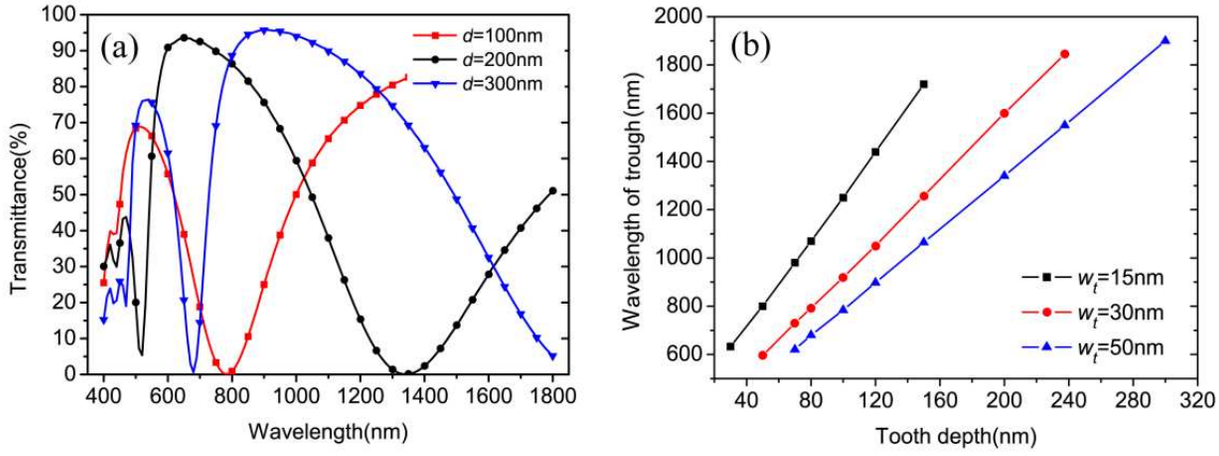

Figure 5. (a) Transmission spectra of the waveguide filters with different tooth depths of d, and with a given tooth width of w_t=50nm and the slit width of w=50nm. (b) The wavelength of the transmission dip vs. the tooth depth of d with w_t=15nm, w_t=30nm and w_t=50nm.

3. Double-side teeth-shaped nano-plasmonic waveguide filters [21]

Figure 6(a) shows the structure of a proposed double-side teeth-shaped waveguide filter. The waveguide width w and the distance L are fixed to be 50nm and 300 nm. d_1 and d_2 are the depths of the teeth on each side of a MIM waveguide. The transmission spectra of the double-side teeth-shaped waveguide filter and the single-side tooth-shaped waveguide filter are shown in Fig. 6(b), which is obtained with the FDTD method. One can see that there is one dip at the free-space wavelength of nearly 1550nm with the transmittance of ~0%. An analytic model to explain the filtering function of single-side tooth-shaped waveguide structure based on multiple-beam-interference and scattering matrix has been given in the section 1

It can be seen that the wavelength λ_m is linear to the tooth depth d and depends on tooth width w through the somewhat inverse-proportionlike relationship between n_{eff} and w shown in Fig. 1. The dip width of the double-side structure is wider compared with that of the single-side tooth-shaped structure. For better understanding the characteristics of double-side teeth structure, we next discuss the dependence of its filtering spectrum on the symmetry of teeth depth.

Figure 7 shows the transmission spectra of the double-side teeth-shaped waveguide filters with different teeth depths of d_1 and d_2. From Fig. 7(a), one can see that there are two transmission dips at the free-space wavelengths of nearly 790nm and 1230nm with d_1=100nm and d_2=180nm. It is found that the wavelength of the second dip shifts to a long wavelength with the increasing of d_2 while the first trough keeps unchanged due to a fixed value of d_1=100nm. From Fig. 7(b), we can see that the first dip shifts to a long wavelength with the increasing of d_1 while the position of the second dip is fixed due to a given d_2=180nm.

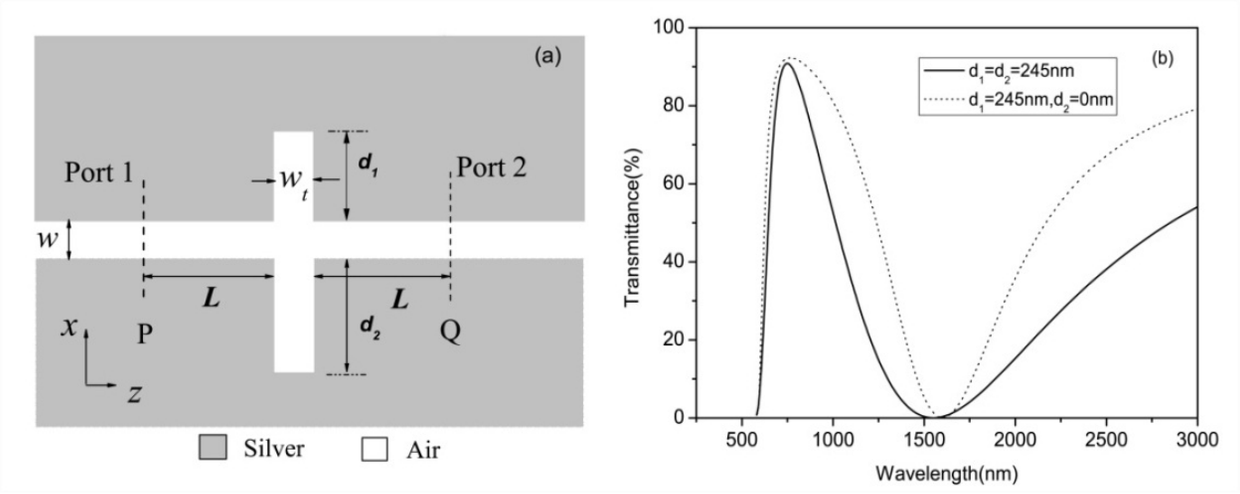

Figure 6. (a) Schematic of a double-side teeth-shaped nano-plasmonic waveguide. The double-side teeth-shaped structure can be asymmetrical, if $d_1 \neq d_2$. (b) The transmission spectra of a symmetrical double-side teeth-shaped waveguide filter with w_t=50nm, d_1=d_2=245nm and a single-side tooth-shaped waveguide filter with w_t=50nm, d_1= 245nm.

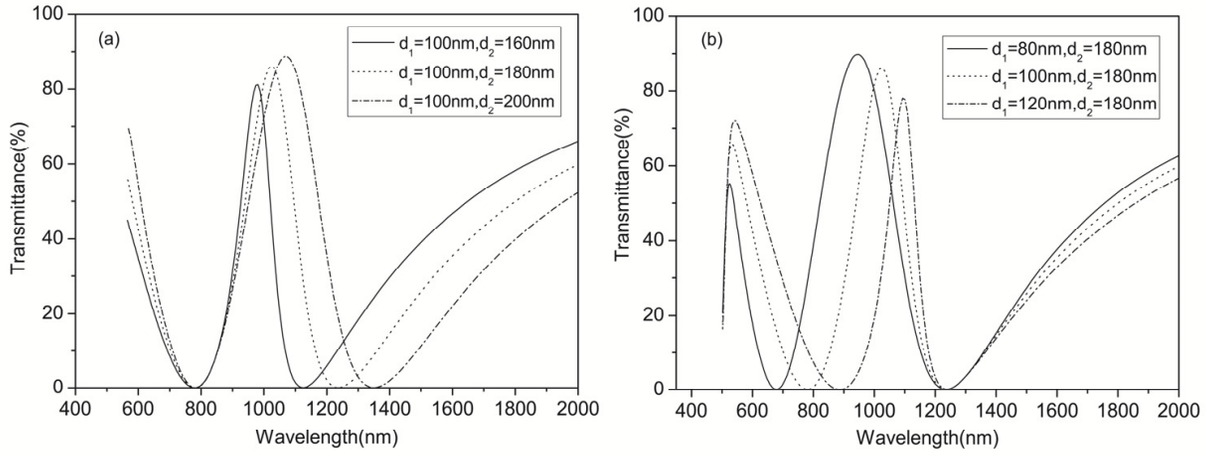

Figure 7. (a)Transmission spectra of the asymmetrical double-side teeth-shaped waveguide filters for different tooth depths of d_2 with a fixed d_1=100nm and w_t=50nm. (b) Transmission spectra of the asymmetrical double-side teeth-shaped waveguide filters for different tooth depths of d_1 with a fixed d_2=180nm and w_t=50nm.

To better understand the origin of the two dips, the transmission spectra of an asymmetrical double-side teeth-shaped waveguide filter with d_1=100nm and d_2=180nm and two single tooth shaped structures with the tooth depths of 100nm and 180nm are all shown in Fig. 8. From it, one can see that the trough positions of the two single tooth waveguide filters with the tooth depths d_1=100nm and d_2=0 as well as d_1=0 and d_2=180nm overlap with the positions of the dips of the asymmetrical double-side teeth-shaped structure, which means the positions of the two dips of the double-side teeth-shaped structure are almost respectively determined by its two different single-tooth parts. Therefore, one can realize the filter function in various required wavelengths by respectively changing the depths of d_1 and d_2 of the two single teeth.

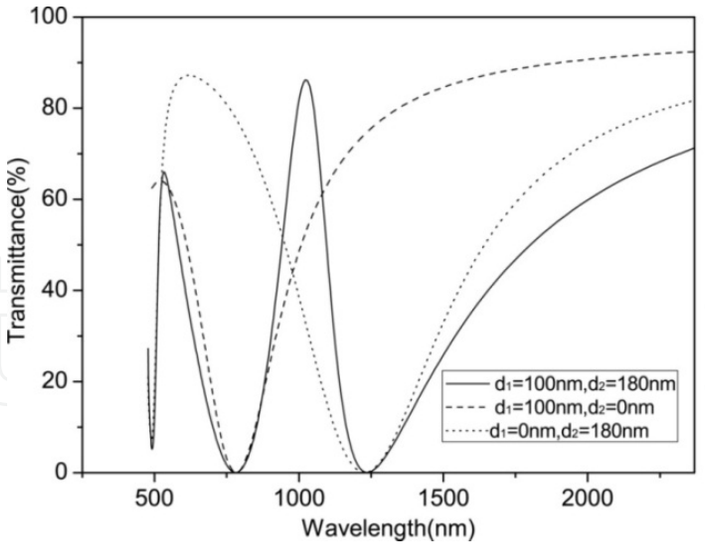

Figure 8. Transmission spectra of the two single-tooth waveguide filters and an asymmetrical double-side teeth-shaped structure with a given tooth width of w_t=50nm and a slit width of w=50nm.

It is also interest to address a staggered double-side teeth-shaped MIM waveguide structure (shown in Fig. 9(a)). L_s stands for the shift length between two single teeth. A typical transmittance of the staggered double-side teeth-shaped waveguide filter with w_t=50nm, d_1=d_2=260.5nm, and L_s =250nm is shown in Fig. 9(b). A wide bandgap occurs around λ=1700nm with the bandgap width (defined as the difference between the two wavelengths at of which the transmittance is equal to 1%) is 660nm, and the transmittance of passband is over 85%. The filter's feature can be attributed to the interference superposition of the reflected and transmitted fields from each tooth of the double-side structure.

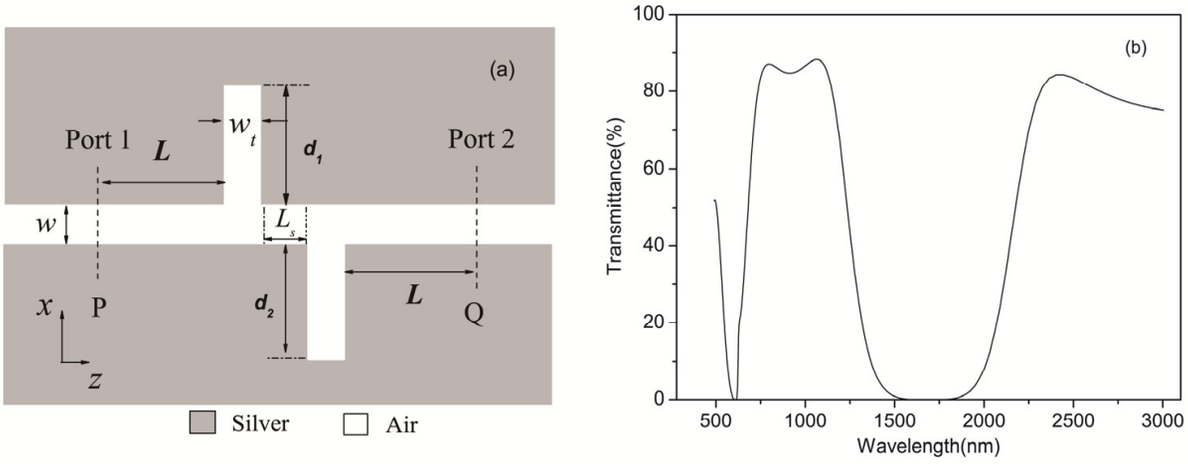

Figure 9. (a) Schematic of a staggered double-side teeth-shaped nano-plasmonic waveguide with a shift length of L_s. (b) The transmittance of the staggered double-side teeth-shaped waveguide filter with w_t=50nm, d_1=d_2=260.5nm, L_s=250nm.

Figure 10 shows the central wavelength of the bandgap as a function of the double-side teeth depth of d. During the simulation, we set d=d_1=d_2. The FDTD simulation results reveal

that the relationship between the central wavelength of the bandgap and the double-side teeth depth of d is a linear function. It reveals that the central wavelength of the bandgap shifts toward long wavelength with the increasing of the teeth depth of d.

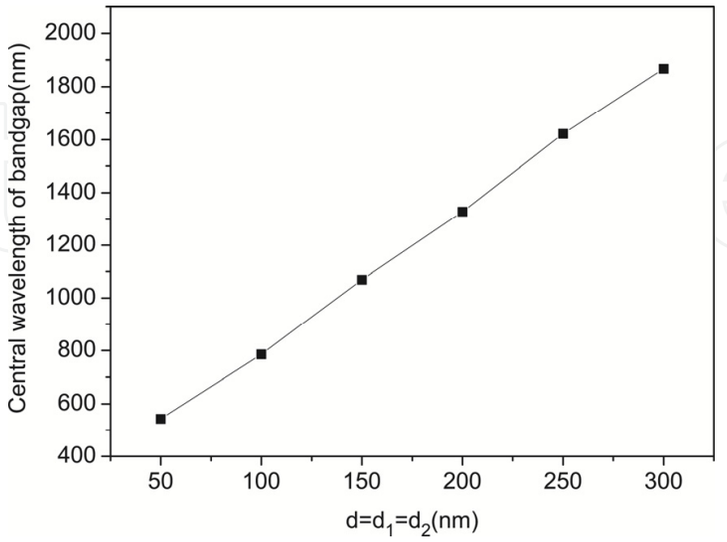

Figure 10. The central wavelength of the bandgap as a function of the double-side teeth depth of d at teeth width of 50nm.

Figure 11 shows how the shift length of the teeth influences or modifies the filtering spectrum of the structure. One can see that central bandgap shifts left and becomes wider with increasing the shift length of L_s. It reveals the filtering characteristics of the structure depend on the phase difference between the plasmon waves passing through the tooth. The optimized filtering response with a sharp left band-edge and high passband-transmittances over 85% can be achieved when the shift length is around 200nm.

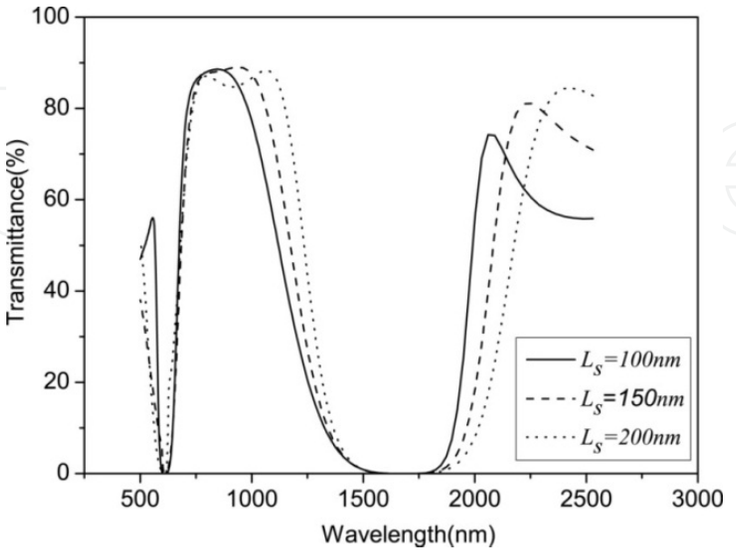

Figure 11. The transmittance of the two-sided staggered teeth-shaped waveguide filter for different shift lengths with w_t=50nm, d_1=d_2=260.5nm.

4. A multiple-teeth-shaped waveguide bandgap filter [22]

It is straight forward and basic interest to expand a single tooth structure to multiple-teeth structure (shown in Fig. 12(a)), and check the difference between them. For the sake of comparison, the waveguide width w and the distance L are fixed to be 50nm and 300nm. Λ and N are the period and the number of rectangular teeth, respectively. w_{gap} stands for the width of the gap that between any two adjacent teeth, and one has $w_t + w_{gap} = \Lambda$. A typical transmittance of the multiple-teeth-shaped waveguide filter with w_t=50nm, Λ=150nm, d=260.5nm and N=5 is shown in the Fig. 12(b), which is obtained with FDTD method. A wide bandgap occurs around λ =1.55μm with the bandgap width 590nm, and the transmittance of passband is over 90%. The filter's feature can be attributed to the superposition of the reflected and transmitted fields from each of the five single tooth-shaped components. Figure 13(a) shows the central wavelength of the transmittance bandgap, while the right y-axis displays the bandgap width of the waveguide filter as a function of teeth depth d at various w_t with the same Λ=150nm and N=5. The FDTD simulation results reveal that the relationship between the central wavelength of the bandgap and the teeth depth d is a linear function for any w_t, which is indeed the one of expectations in Eq. (9). Figure 13(b) shows the central wavelength of the bandgap and the bandgap width as a function of teeth width of w_t at various teeth depths. As revealed in the Eq. (9), the relationship between the bandgap position and w_t mainly results from the contribution of the inverse-proportion-like dependence of n_{eff} on w_t as shown in Fig. 1(a). Obviously, teeth width w_t should be chosen within the range of 50-100nm with a slope of $d\lambda_{center} / dw_t \approx 5$ to avoid a large value of $d\lambda_{center} / dw_t \approx 20$ when w_t <45nm in Fig. 13(b), and to reduce the sensitivity of the central wavelength of bandgap in fabrication process. Therefore, one can realize the filter function at various required wavelengths with high performance, by choosing the width or/and the depth of the teeth.

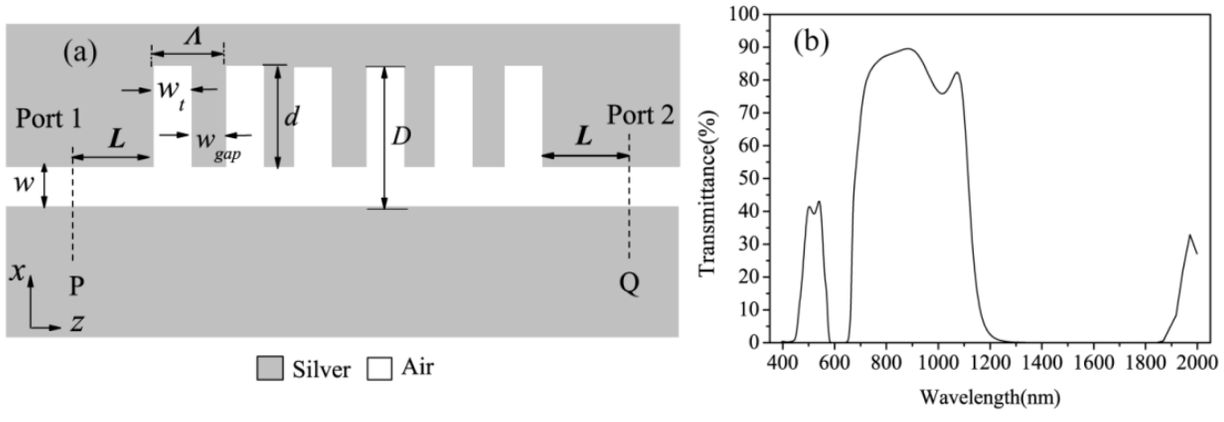

Figure 12. (a) Schematic of a multiple-teeth-shaped MIM waveguide structure. (b) The transmittance of the multiple-teeth-shaped waveguide filter with w_t=50nm, Λ=150nm, d=260.5nm and N=5.

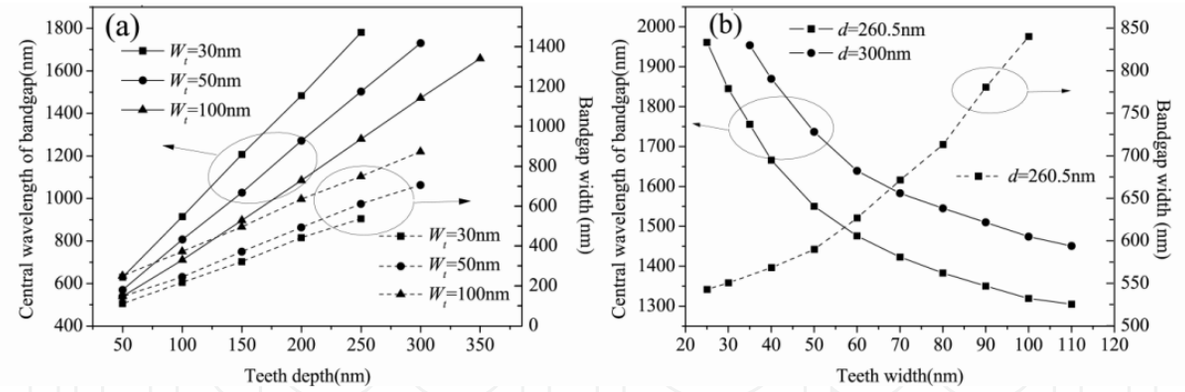

Figure 13. (a) The central wavelength of the bandgap and the bandgap width as a function of the teeth depth of d at various teeth widths. (b) The central wavelength of the bandgap and the bandgap width as a function of teeth widths of w_t at various teeth depths.

For the multiple-teeth-shaped structure with the parameters of $n_{eff,teeth} = 1.070$ for the width of D=d+w=(260.5+50)nm, $n_{eff,wg} = 1.375$ for w=50nm, and the teeth period of $\Lambda = w_t + w_{gap} = 150\text{nm}$ in z-axis direction, one can see $w_t \,\mathrm{Re}(n_{eff,teeth}) + w_{gap}\,\mathrm{Re}(n_{eff,wg}) \approx 401.1\text{nm} < 1550\text{nm}/2$. Thus the structure does not follow the Bragg condition in z-axis direction.

Figure 14(a) and (b) show the transmission spectra of a multiple-teeth-shaped waveguide filter at different periods Λ and period numbers N. As one can see from Fig. 14(a), when Λ=100nm is chosen, the coupling of the SPPs waves between two adjacent teeth is strong which causes the central bandgap wavelength to shift left and the bandgap to be wider. When the period equals to Λ=200nm, the coupling between any two adjacent teeth becomes very weak. One can see in Fig. 14(b) that, the forbidden bandwidth increases little with the changing of the period number from N=3 to 7, while the transmittance of the passband decreases from 93% to 86%. The reason for the decreasing in transmittance can be attributed to the increasing of the propagation loss of the lengthened structure with a large period number. From the simulation results, a tradeoff period number N=4 is the optimized number with the transverse filter length of 4×150nm, which is ~5 times shorter than the previous grating-like filter structures.

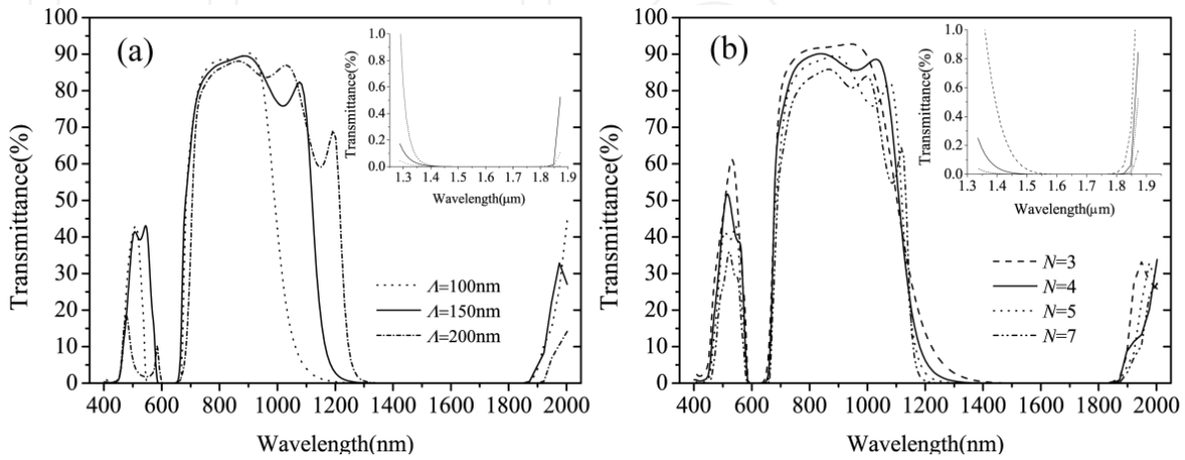

Figure 14. (a) Transmittance spectra of multi-teeth filters with different periods and a fixed N=5, (b) Transmittance spectra of multi-teeth filters consisting of 3-7 periods with a fixed Λ=150nm.

5. A narrow band subwavelength plasmonic waveguide filter with asymmetrical multiple teeth-shaped structure [23]

The asymmetrical multiple-teeth-shaped structure is shown in Fig. 15(a), which is composed of two sets of multiple-teeth with two different teeth depths. The short set has three teeth, and the long set has four teeth. Λ, N_1 and N_2, are the period, the numbers of short rectangular teeth and long teeth, respectively. w_{gap} stands for the width of the gap between any two adjacent teeth in multiple-teeth structure, and one has $w_t + w_{gap} = \Lambda$. The separation between the 3rd short tooth and 1st long tooth is w_s. The length of L and the waveguide width w are, respectively, fixed to be 150nm and 50nm. In Fig. 15(a) we set d_1=148nm, d_2=340nm, w_t=50nm, w_{gap}= w_s =84nm. Figure 15(b) shows a typical transmission spectrum of the asymmetrical multiple-teeth-shaped structure using FDTD method.

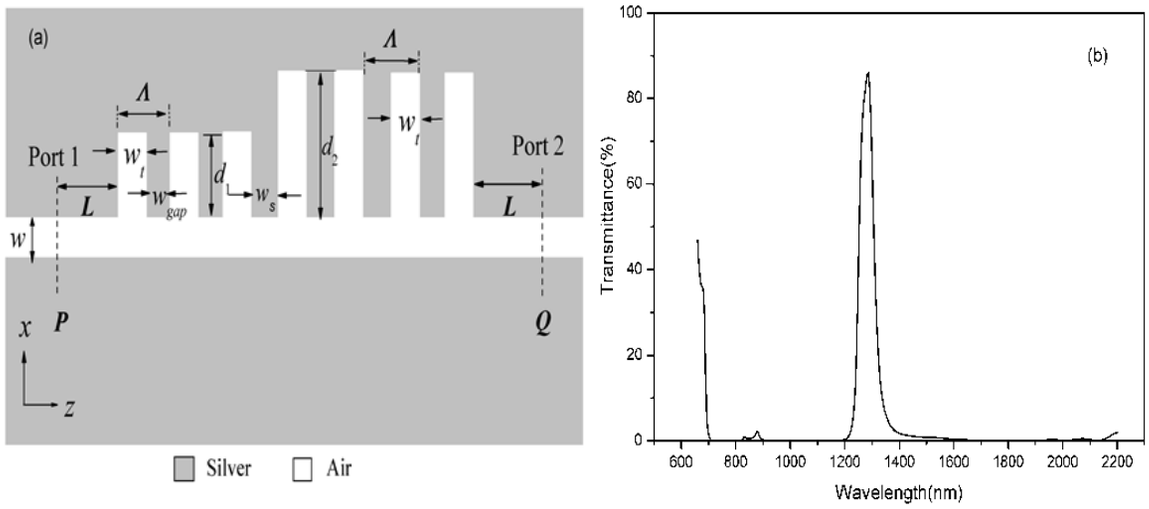

Figure 15. (a) Schematic of an asymmetrical multiple-teeth structure consisted of two sets with different teeth depth. (b) The transmittance of the asymmetrical multiple-teeth-shaped waveguide filter with d_1=148nm, d_2=340nm. w_{gap}= w_s =84nm, N_1=3, and N_2=4.

One can see the maximum transmittance at the wavelength of 1287nm is nearly 90%, and the full-width at half-maximum (FWHM) is nearly 70nm which is much smaller than the bandgap width of 1300nm. The FWHM of the asymmetrical multiple-teeth-shaped structure is also smaller than our previous coupler-type MIM optical filter [24].

In order to understand the origin of the narrow passband of the structure, the spectra of the transmission of a single-set of short three-teeth structure and a single-set of long four-teeth structure are calculated, and shown in Fig. 16. The parameters of the two structures are respectively equal to the parameters of the short teeth part and the long teeth part of the asymmetrical multiple-teeth-shaped structure (shown in Fig. 15(a)). One can see that the passband (or the bandgap) of the long teeth structure and the bandgap (or the passband) of the short teeth are overlapped from 800nm to 1200nm (or from 1450 to 1800nm), and then the transmission of the cascade of the two structure is very low within the two regions. Only the overlapping between the right edge of the passband of the long teeth structure and the

left passband of the short teeth is non-zero. This is the reason why the wavelengths around 1300nm have a transmission peak in Fig. 15 (b).

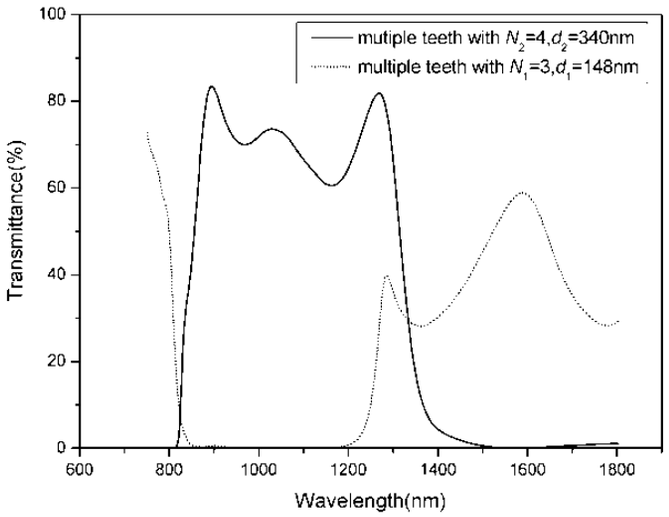

Figure 16. The transmission spectra of the single-set of multiple-teeth structure with d_1=148nm, N_1=3 and the single set of multiple-teeth structure with d_2=340nm, N_2=4, respectively.

Figure 17 shows the central wavelength of the narrow-band as a function of the variation of $\Delta d=\Delta d_1=\Delta d_2$. Δd is the increment of d_1 and d_2. The initial values of d_1 and d_2 are respectively, 128nm and 320nm. From the Fig. 17 can see that the central wavelength of the narrow-band linearly increases with the simultaneous increasing of d_1 and d_2. Figure 18 shows the dependence of transmission characteristic on separation w_s. It is found that the transmission at the wavelength of 1287nm reaches the peak value when the separation of w_s equals the gap of w_t. Therefore, one can realize the narrow-bandwidth filter function at different required wavelengths by means of properly choosing the parameters of the device, such as the teeth-depth, the period or the separation of w_s.

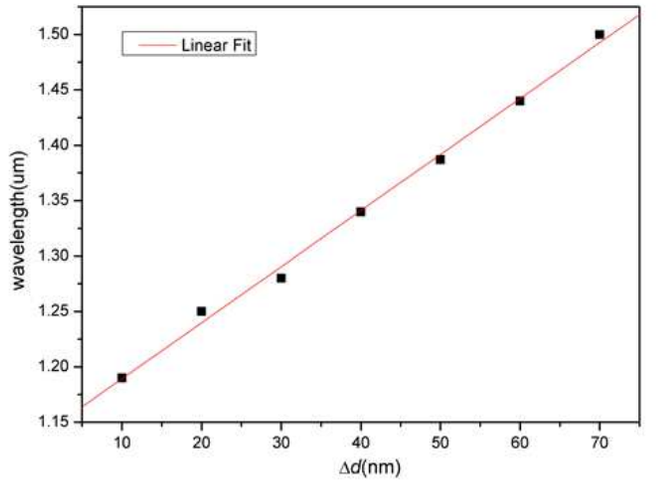

Figure 17. Central wavelength of the narrow-band as a function of the variation of $\Delta d=\Delta d_1=\Delta d_2$, $\Delta d_1$and Δd_2 are respectively the increment of d_1 and d_2.

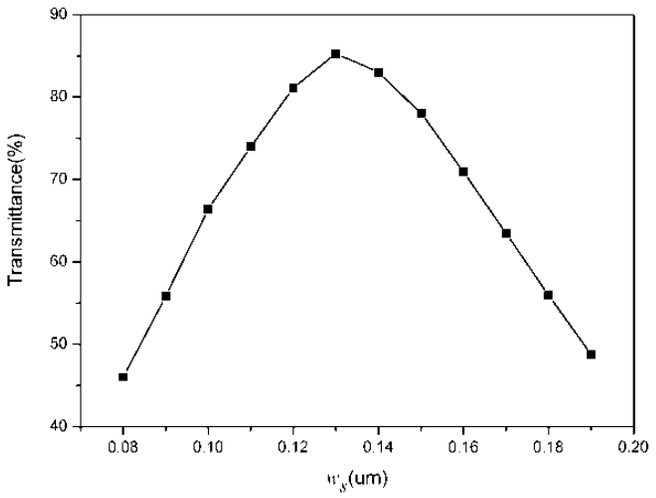

Figure 18. Dependence of transmission characteristic on separation between the 3rd short tooth and the 1st long tooth with d_1=148nm, N_1=3, d_2=340nm, N_2=4, respectively.

6. A wavelength demultiplexing structure based on metal-dielectric-metal plasmonic nano-capillary resonators [25].

The inset of Fig. 19 shows the nano-capillary resonators composed of two parallel metal plates with a dielectric core. Obviously, the structure can be treated as two MDM waveguides with different widths. Because the width of the lower MDM waveguide is much smaller than that of the upper part, here we call the lower (narrower) part as a nano-capillary. When the gap width w of the MDM waveguide is reduced below the diffraction limit, only a single propagation mode TM_0 can exist. The dielectric in the core of the structure is assumed to be air with a permittivity ε_d=1.

To fully understand how the width of the nano-capillary structure influences the SPPs propagation, the dependences of the effective index of SPPs on the width w at various wavelengths of the incident light are calculated and shown in Fig. 19. From the figure 19, one can see that the effective index of the waveguide decreases with increasing of w at the same wavelength. The effective index at short wavelength is larger than that at long wavelength, for a given width w. The effective index n_{eff2} of the nano-capillary can be larger than n_{eff3} of upper MDM part and n_1 of air. As shown in inset of Fig. 19, the waves will flow into the nano-capillary due to its higher effective index, when SPP waves propagate along the interface between metal and air. The wave transmitted into the capillary will be partly reflected at two ends of nano-capillary, because of index differences between n_{eff2} and n_{eff3} as well as n_1. One can expect the nano-capillary operates as a resonator. Resonance waves can

be formed only in some appropriate conditions within nano-capillary segment. Defining $\Delta\phi$ to be the phase delay per round-trip in the nano-capillary, one has $\Delta\phi = 4\pi n_{eff} d / \lambda + \phi_r$, where $\phi_r \equiv \phi_1 + \phi_2$, ϕ_1 and ϕ_2 are respectively the phase shifts of a beam reflected on the entrance of the capillary and the junction connecting the nano-capillary and the upper MDM waveguide, and d is the length of the capillary. The waves propagating through the structure will be trapped within the nano-capillary when the following resonant condition is satisfied: $\Delta\phi = m \cdot 2\pi$. Here, positive integer m is the number of antinodes of the standing SPP wave. The resonant wavelengths can be obtained as follows:

$$\lambda_m = 2n_{eff} d / (m - \phi_r / \pi). \tag{10}$$

It can be seen that the wavelength λ_m is linear to the length and the effective index of the nano-capillary, respectively. Obviously, only the waves with the wavelength λ_m can stably exist in the nano-capillary, and thus partly transmit or drop into the output end of the nano-capillary. When wideband SPP waves incident into the structure, only the resonance waves with the wavelength λ_m can be selected and dropped by the nano-capillary. In other words, a transmission peak with the wavelength λ_m will be formed in the output section.

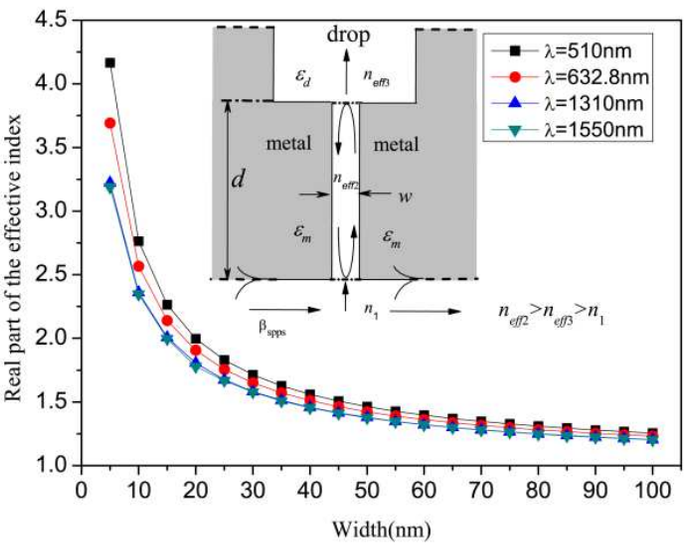

Figure 19. Dependence of real part of the effective index of SPPs in a plasmonic MDM waveguide on wavelength of the incident light and width w. Inset: schematic picture of a MDM nano-capillary resonator.

Fig. 20(a) shows a typical schematic of a 1×3 wavelength demultiplexing structure based on MDM nano-capillary resonators. The wavelength demultiplexing structure consists of three nano-capillary resonators perpendicularly connected to a bus waveguide. w_1 and d_1 stand for the width and the length of the first nano-capillary, respectively. Since the width of the bus waveguide is much smaller than the operating wavelength in the structure, only the excitation of the fundamental waveguide mode is considered. The incident light used to excite SPP wave is a TM-polarized (the magnetic field is parallel to y axis) fundamental mode. In the following FDTD simulation, the grid sizes in the x and the z directions are chosen to be Δx = 5 nm, Δz = 1.5 nm. Power monitors are respectively set at the positions of P and Q to detect the incident power of P_{in} and the transmitted power of P_{out}. The transmittance is defined to be $T = P_{out} / P_{in}$. The width w' of the bus waveguide is set to be 250 nm while the length of L_1 and L_2 are fixed to be 50 nm and 500 nm. As an example, three nano-capillaries have been designed to split the first, the second and third optical transmission windows, although more nano-capillaries can be added. The parameters of the structure are set to be w = 15 nm, w_1 = 250 nm, d_1 = 202 nm, d_2 = 290 nm, and d_3 = 347 nm in calculation. Fig. 20(b) shows the transmission spectra at the outputs of the three channels, and inset of fig. 20(b) shows transmittance and reflectance of the bus waveguide. From it, one can see channels l-3 can select 980 nm, 1310 nm, 1550 nm bands, respectively, and the maximum transmittance in three bands can exceed 30% (-5.2 dB). And there is also another high transmission in channel 3 around 820 nm wavelength for m = 2. Given the total phase shift ϕ_r, one can estimate the resonance wavelength from Eq. (10). Submitting λ_m = 1310 nm into Eq. (10) gives ϕ_r = 0.35 for d = 290 nm and n_{eff} = 2.01. Other resonance wavelengths can be approximately calculated with the formula. For the lengths of the nano-capillaries of 347 nm and 202 nm, resonance wavelengths are simply estimated to be 1559 nm and 926 nm. The deviation between FDTD simulation and the result from Eq. (10) could be partly attributed to the neglecting of wavelength dependence of ϕ_r. And it is partly due to the fact that Eq. (10) is derived based on the effective index approximation that SPP waves with the phase factor of $\exp(i2\pi n_{eff} x / \lambda)$ travel back and forth within a capillary, similar to a 3-dimentional plane wave with $\exp(i2\pi n x / \lambda)$ traveling in a bulk medium with refractive index n.

The FWHM of channel 1-3 are 75 nm, 130 nm, 160 nm, respectively. Obviously, the FWHM of the channel 2 and channel 3 are larger than that of channel 1. The reason is that, from the calculation in Fig. 19, the effective index at short wavelength with a fixed width of nano-capillary is higher compared with the one at long wavelength, thus the waves at short wavelength have a higher reflectivity at two ends of nano-capillary and its Q factor is higher. Cross-talk is defined as the ratio between the power of the undesired and desired bands at the outputs. The cross-talk between channel 1 and channel 2 is around -19.7 dB for the 980 nm branch, and the cross-talk between them is -13.1 dB for the 1310 nm branch. The cross-talk between channel 1 and the whole channel 3 is around -19.2 dB for the 980 nm branch, and is -16.6 dB for the 1550 nm branch, although there is also another high

transmission in channel 3 around 820nm wavelength for m=2. Therefore, this structure is suitable for wideband wavelengths demultiplexing.

Equation (10) indicates that the transmission behavior of each nano-capillary (channel of the demultiplexing structure) mainly depends on two parameters: the length of the nano-capillary, and the effective index of SPPs in the nano-capillary, which is determined by its width. Figure 21 shows the central wavelength of the nano-capillary resonator as a function of nano-capillary length d. One can see that the central wavelength of nano-capillary shifts toward longer wavelengths with the increasing of nano-capillary length d, as expected from equation (10). Therefore, one can realize the demultiplexing function at arbitrary wavelengths through the nano-capillary resonator by means of properly choosing the parameters of the structure, such as nano-capillary length and width.

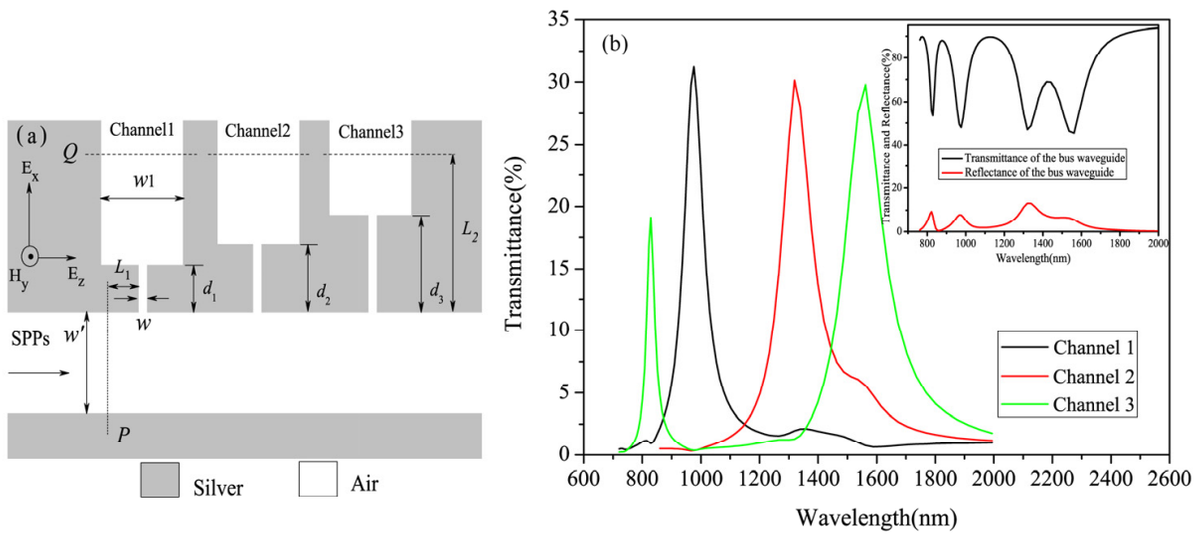

Figure 20. (a) Schematic of a 1×3 wavelength demultiplexing structure based on MDM plasmonic nano-capillary resonators. (b) Transmission spectra of the three channels of the demultiplexing structure with w = 15 nm, w_1 = 250 nm, d_1 = 202 nm, d_2 = 290 nm and d_3 = 347 nm. Inset: Transmittance and reflectance of the bus waveguide.

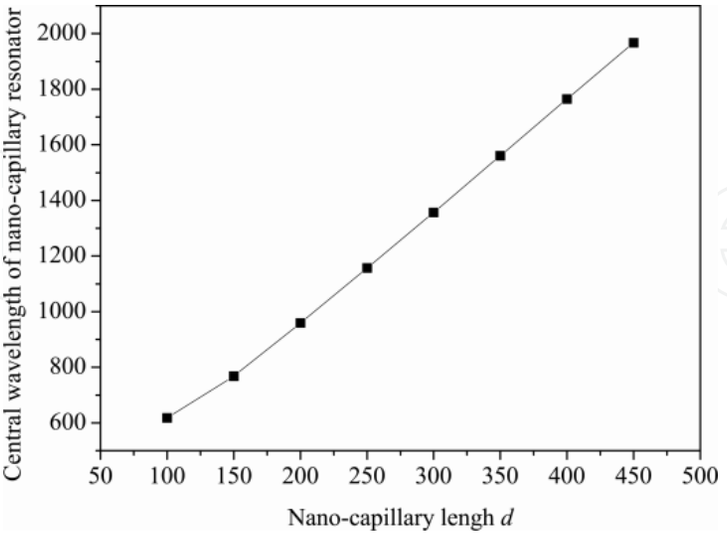

Figure 21. The central wavelength of nano-capillary resonator as a function of nano-capillary length d.

Finally, Figure 22 shows the propagation of field H_y for two monochromatic waves with different wavelengths of 980 nm and 1550 nm launched into nano-capillary resonator demultiplexing structure. The demultiplexing effect is clearly observed. From the figure, one can see the wave with wavelength of 980 nm passing through the first nano-capillary and the wavelength of 1550 nm wave transmitting from the third nano-capillary. This is in good agreement with the transmission spectra shown in Fig. 20(b).

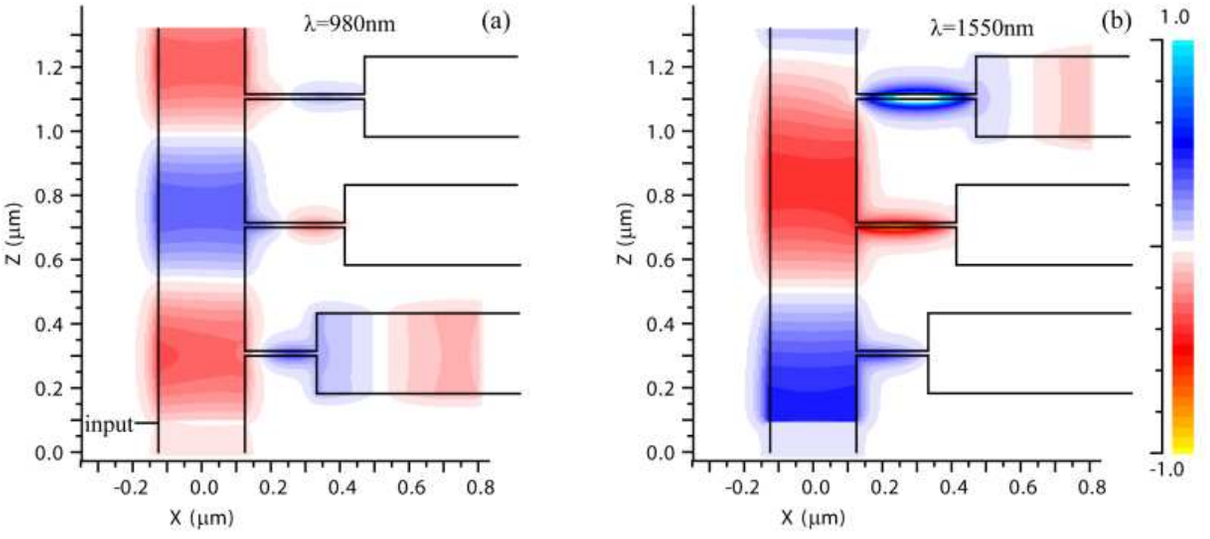

Figure 22. The contour profiles of field H_y of the 1×3 wavelength demultiplexing structure at different wavelengths, (a) λ = 980 nm, (b) λ = 1310 nm. All parameters of the structure are same as in Fig. 2(b).

7. Conclusion

In this chapter, we present our work on nano-plasmonic waveguide filters based on tooth/teeth-shaped and nano-capillary structures. We firstly investigated a novel plasmonic waveguide filter constructed with a MDM structure engraved single rectangular tooth. The filter is of an ultra-compact size with a few hundreds of nanometers in length, with reducing fabrication difficulties, compared with previous grating-like heterostructures with a few micrometers in length. We then extended it to symmetric/asymmetric multiple-teeth, capillary structures. The asymmetrical multiple-teeth structure and the capillary structure can achieve selective narrow-band filtering and wavelength demultiplexing functions, respectively. The plasmonic filters might become a choice for the design of all-optical high-integrated architectures for optical computing and communication in nanoscale. In the future, it will be very interesting and usefully to find some solutions to improve the performance of the MIM/MDM plasmonic components. Such as to combine surface plasmons with electrically and optically pumped gain media such as semiconductor quantum dots, semiconductor quantum well, and organic dyes embedded to the dielectric part. Electrically and optically pumped semiconductor gain media and the emerging technology of graphene are also expected to provide loss compensation from visible to terahertz spectra range [26].

Author details

Xu Guang Huang* and Jin Tao
Key Laboratory of Photonic Information Technology of
Guangdong Higher Education Institutes, South China Normal University, Guangzhou, China

Acknowledgement

The authors acknowledge the financial support from the National Natural Science Foundation of China (Grant No. 11977866).

8. References

[1] J. Davis, R. Venkatesam, A. Kaloyeros, M.Meylansky, S. Souri, K. Banerjee, K. Saraswat, A. Rahman, R. Reif, J. Meidl, "Interconnect Limits on Gigascale Integration (GSI) in the 21st Century," Proceedings of the IEEE, Vol. 89, 305-324 (2001).

[2] J. A. Conway, S. Sahni, and T. Szkopek, "Plasmonic interconnects versus conventional interconnects: a comparison of latency, crosstalk and energy costs," Opt. Express, Vol. 15, 4474-4484 (2007).

[3] P. Bhattacharya. Semiconductor Optoelectronic Devices. Second Edition. © 2005 Prentice-Hall of India, New Dehli – 110 001. pg. 102.

[4] E. Yablonovitch, "Inhibited Spontaneous Emission in Solid-State Physics and Electronics," Phys. Rev. Lett 58, Vol. 20, 2059–2062 ,1987.

* Corresponding Author

[5] S. John, "Strong localization of photons in certain disordered dielectric superlattices," Phys. Rev. Lett, Vol. 58 , 2486–2489 ,1987.
[6] Maier, S. A. et al. "Local detection of electromagnetic energy transport below the diffraction limit in metal nanoparticle plasmon waveguides," Nature Mater., Vol. 2, 229–232, 2003.
[7] W. Saj, "FDTD simulations of 2D plasmon waveguide on silver nanorods in hexagonal lattice," Opt. Express, Vol. 13, 4818-4827, 2005.
[8] S. I. Bozhevolyni, V. S. Volkov, E. Devaux, and T. W. Ebbesen, "Channel plasmon–polariton guiding by subwavelength metal grooves," Phys. Rev. Lett., Vol. 95, 046802, 2005.
[9] K. Tanaka, M. Tanaka, and T. Sugiyama, "Simulation of practical nanometric optical circuits based on surface plasmon polariton gap waveguides," Opt. Express, Vol. 13, 256–266, 2005.
[10] J. R. Krenn et al. "Non-diffraction-limited light transport by gold nanowires," Europhys Lett., Vol. 60, 663–669, 2002.
[11] B. Wang and G. Wang, "Plasmon Bragg reflectors and nanocavities on flat metallic surface," Appl. Phys. Lett., Vol. 87, 013107, 2005.
[12] A. Boltasseva, S. I. Bozhevolnyi, T. Nikolajsen, and K. Leosson, "Compact Bragg gratings for Long-Range surface plasmon polaritons," J. Lightwave Technol. Vol. 24, 912-918, 2006.
[13] A. Hossieni and Y. Massoud, "A low-loss metal-insulator-metal plasmonic bragg reflector," Opt. Express, Vol. 14, 11318-11323, 2006.
[14] A. Hosseini, H. Nejati, and Y. Massoud, "Modeling and design methodology for metal-insulator-metal plasmonic Bragg reflectors," Opt. Express, Vol. 16, 1475-1480, 2008.
[15] J. Park, H. Kim, and B. Lee, "High order plasmonic Bragg reflection in the metal-insulator-metal waveguide Bragg grating," Opt. Express, Vol. 16, 413-425, 2008.
[16] Z. Han, E. Forsberg, and S. He, "Surface plasmon Bragg gratings formed in metal-insulator-metal waveguides," IEEE Photon.Technol. Lett, Vol. 19, 91-93, 2007.
[17] Xian Shi Lin and Xu Guang Huang, "Tooth-shaped plasmonic waveguide filters with nanometeric sizes," Opt. Lett, Vol. 33, 2874-2876, 2008.
[18] J. A. Dionne, L. A. Sweatlock, and H. A. Atwater, "Plasmon slot waveguides: Towards chip-scale propagation with subwavelength-scale localization," Phys. Rev. B., Vol 73, 035407 (2006).
[19] E. D. Palik, Handbook of optical constants of *solids* (Academic Press, New York, NY 1985).
[20] H. A. Haus, Waves and Fields in Optoelectronics (Prentice-Hall, Englewood Cliffs, NJ, 1984).
[21] J. Tao, Xu Guang Huang, X. S. Lin, et al, "Systematical research on characteristics of double-sided teeth-shaped nanoplasmonic waveguide filters," J. Opt. Soc. Am. B, Vol. 27, 323-327, 2010.
[22] X. S. Lin and X. G. Huang, "Numerical modeling of a teeth-shaped nanoplasmonic waveguide filter," J. Opt. Soc. Am. B, Vol. 26, 1263-1268, 2009.

[23] J. Tao, X. G. Huang, X. S. Lin, Q. Zhang, X. P, Jin, "A narrow-band subwavelength plasmonic waveguide filter with asymmetrical multiple-teeth-shaped structure," Opt. Express, Vol. 17, 13989-13994, 2009.
[24] Qin Zhang, Xu-Guang Huang, Xian-Shi Lin, Jin Tao, and Xiao-Ping Jin, "A subwavelength coupler-type MIM optical filter," Opt. Express, Vol. 17, 7549-7555, 2009.
[25] Jin Tao, Xu Guang Huang, and Jia Hu Zhu, "A wavelength demultiplexing structure based on metal-dielectric-metal plasmonic nano-capillary resonators," Opt. Express, Vol. 18, 11111-11116, 2010.
[26] A. A Dubinov, V. Y. Aleshkin, V. Mitin, T. Otsuji and V. Ryzhii, "Terahertz surface plasmons in optically pumped graphene structures," J. Phys.Condens. Matter, Vol. 23, 145302 2011.